1	Molecular Dynamics Simulations of Polyelectrolyte Complexes
2	Tania Rajpersaud ¹ , Sara Tabandeh ² , Lorraine Leon ² , Sharon M. Loverde ^{1,3,4,5,*}
3 4	¹ Ph.D. Program in Biochemistry, The Graduate Center of the City University of New York, New York, NY, 10016, United States
5 6	² Department of Materials Science and Engineering, University of Central Florida, 4000 Central Florida Boulevard, Orlando, Florida, 32816, United States
7 8	³ Department of Chemistry, College of Staten Island, The City University of New York, 2800 Victory Boulevard, Staten Island, New York, 10314, United States
9 10	⁴ Ph.D. Program in Chemistry, The Graduate Center of the City University of New York, New York, NY, 10016, United Sdtates
11 12	⁵ Ph.D. Program in Physics, The Graduate Center of the City University of New York, New York, NY, 10016, United States
13 14	E-mail: sharon.loverde@csi.cuny.edu , Phone: 718-982-4075 , Fax: 718-982-4075 ,
15 16	Abstract
17	Polyelectrolyte complexes (PECs) are currently of great interest due to their applications towards
17 18	Polyelectrolyte complexes (PECs) are currently of great interest due to their applications towards developing new adaptive materials and their relevance in membrane-less organelles. These com-
18	developing new adaptive materials and their relevance in membrane-less organelles. These com-
18 19	developing new adaptive materials and their relevance in membrane-less organelles. These complexes emerge during phase separation when oppositely charged polymers are mixed in aqueous
18 19 20	developing new adaptive materials and their relevance in membrane-less organelles. These complexes emerge during phase separation when oppositely charged polymers are mixed in aqueous media. Peptide-based PECs are particularly useful towards developing new drug delivery methods
18 19 20 21	developing new adaptive materials and their relevance in membrane-less organelles. These complexes emerge during phase separation when oppositely charged polymers are mixed in aqueous media. Peptide-based PECs are particularly useful towards developing new drug delivery methods due to their inherent biocompatibility. The underlying peptide sequence can be tuned to optimize
18 19 20 21 22	developing new adaptive materials and their relevance in membrane-less organelles. These complexes emerge during phase separation when oppositely charged polymers are mixed in aqueous media. Peptide-based PECs are particularly useful towards developing new drug delivery methods due to their inherent biocompatibility. The underlying peptide sequence can be tuned to optimize specific material properties of the complex, such as interfacial tension and viscosity. Given their
18 19 20 21 22 23	developing new adaptive materials and their relevance in membrane-less organelles. These complexes emerge during phase separation when oppositely charged polymers are mixed in aqueous media. Peptide-based PECs are particularly useful towards developing new drug delivery methods due to their inherent biocompatibility. The underlying peptide sequence can be tuned to optimize specific material properties of the complex, such as interfacial tension and viscosity. Given their applicability, it would be advantageous to understand the underlying sequence-dependent phase
18 19 20 21 22 23 24	developing new adaptive materials and their relevance in membrane-less organelles. These complexes emerge during phase separation when oppositely charged polymers are mixed in aqueous media. Peptide-based PECs are particularly useful towards developing new drug delivery methods due to their inherent biocompatibility. The underlying peptide sequence can be tuned to optimize specific material properties of the complex, such as interfacial tension and viscosity. Given their applicability, it would be advantageous to understand the underlying sequence-dependent phase behavior of oppositely charged peptides. Here, we report microsecond molecular dynamic simu-
18 19 20 21 22 23 24 25	developing new adaptive materials and their relevance in membrane-less organelles. These complexes emerge during phase separation when oppositely charged polymers are mixed in aqueous media. Peptide-based PECs are particularly useful towards developing new drug delivery methods due to their inherent biocompatibility. The underlying peptide sequence can be tuned to optimize specific material properties of the complex, such as interfacial tension and viscosity. Given their applicability, it would be advantageous to understand the underlying sequence-dependent phase behavior of oppositely charged peptides. Here, we report microsecond molecular dynamic simulations to characterize the effect of hydrophobicity on the sequence-dependent peptide confor-
18 19 20 21 22 23 24 25 26	developing new adaptive materials and their relevance in membrane-less organelles. These complexes emerge during phase separation when oppositely charged polymers are mixed in aqueous media. Peptide-based PECs are particularly useful towards developing new drug delivery methods due to their inherent biocompatibility. The underlying peptide sequence can be tuned to optimize specific material properties of the complex, such as interfacial tension and viscosity. Given their applicability, it would be advantageous to understand the underlying sequence-dependent phase behavior of oppositely charged peptides. Here, we report microsecond molecular dynamic simulations to characterize the effect of hydrophobicity on the sequence-dependent peptide conformation for model polypeptide sequences that were previously reported by <i>Tabandeh et al.</i> These
18 19 20 21 22 23 24 25 26 27	developing new adaptive materials and their relevance in membrane-less organelles. These complexes emerge during phase separation when oppositely charged polymers are mixed in aqueous media. Peptide-based PECs are particularly useful towards developing new drug delivery methods due to their inherent biocompatibility. The underlying peptide sequence can be tuned to optimize specific material properties of the complex, such as interfacial tension and viscosity. Given their applicability, it would be advantageous to understand the underlying sequence-dependent phase behavior of oppositely charged peptides. Here, we report microsecond molecular dynamic simulations to characterize the effect of hydrophobicity on the sequence-dependent peptide conformation for model polypeptide sequences that were previously reported by <i>Tabandeh et al.</i> These sequences are designed with alternating chirality of the peptide backbone. We present microsecond

with experimentally reported results. Ramachandran plots reveal that backbone conformation at

the single amino acid level is highly influenced by the neighboring sequence in the chain. These

31

results give insight into how subtle changes in hydrophobic side chain size and chirality influence the strength of hydrogen bonding between the chains and, ultimately, the secondary structure. Furthermore, principal component analysis reveals that the minimum energy structures may be subtly modulated by the underlying sequence.

INTRODUCTION

Polyelectrolyte Complexes (PECs) are a new class of tunable materials that are formed from the complexation of oppositely charged polyelectrolytes in aqueous media. When combined, the oppositely charged polymers can interact to form polymer-rich droplets, which can eventually merge to form a distinct phase of either liquid-like or solid-like character¹. Recently, there has been a strong interest in understanding the dynamics and rheology of PECs due to their ability to self-assemble and respond to external stimuli. The mechanical properties of the formed PECs are defined by a complex combination of external and internal factors, such as the solution pH, temperature, ionic strength, charge density, and molecular weight of the interacting polymers². Generally, the ideal conditions for complexation are based on maximizing the number of interaction opportunities between the oppositely charged polymers. For example, this could mean maximizing the electrostatic interactions by mixing equal parts of oppositely charged polymers in a solution containing no external ions and at a pH that allows the charged groups to be fully ionized^{2d, 3}. Additionally, shorter-range forces such as hydrogen bonds are another means of interaction^{1b, d}. These factors, which affect how the polymers interact, can be used to guide the behavior of PECs towards functional properties.

Complexes with liquid-like properties are referred to as liquid coacervates and are currently being extensively studied due to their low interfacial tension with water, which can be applied to the design of effective drug delivery vehicles⁴ and new biocompatible materials⁵. Further, the process behind the formation of liquid coacervates is currently being applied to explain the function and behavior of membrane-less organelles in cellular biology⁶. Complexes with solid-like properties are often referred to as solid precipitates and, unlike liquid coacervates, they are not as well studied due to their brittle nature, making them difficult to work with. The formation of solid-like complexes usually arises due to strong interactions between the oppositely charged polymers,

which limits the mobility of the constituent polymers and excludes more water than liquid coacervates. Currently, there is an intense interest in understanding the phase behavior of polyelectrolyte complexes to link the primary sequences with macroscopic properties. Peptide-based PECs are a unique option to characterize the relationship between polymer structure and PEC properties, given the ability to design specifically patterned sequences. Further, the chirality of the individual amino acids is another method of guiding the phase behavior of the formed PEC^{1b, 2a}. Studies have shown that alternating chirality along a peptide can help to disrupt backbone hydrogen bonds, limiting the interaction between the constituent peptides in the PEC and allowing the PEC to take on a more liquid-like behavior^{1b, 7}.

1

2

3

4

5

6

7

8

9

10

11

12

13

14

15

16

17

18

19

20

21

22

23

24

25

26

27

28

29

30

The properties of peptide-based PECs can also be modified by the incorporation of hydrophobic residues. Tabandeh et al⁸ directly examined the effect of hydrophobicity on polyelectrolyte complexation by characterizing the stability of six peptide-based polyelectrolyte complexes. These six systems consisted of anionic polyglutamate and cationic polylysine, where the constituent peptides are intervened by either glycine, alanine, or leucine and the adjacent residues are of opposite chirality. When unmixed, these polyelectrolytes are all soluble in water and buffered solutions (at pH 7 it is assumed that the polypeptides are fully charged). Upon mixing, all six systems were observed to form a high-density phase consisting of the oppositely charged peptides where the phase-behavior of the high-density phase was observed to be correlated to the length of the variable side chain. Specifically, they found that the incorporation of longer side chains into the peptide pattern resulted in PECs that were less likely to form solid-like precipitates and concluded that the hydrophobic variable residues could discourage backbone hydrogen bonding and give rise to more liquid-like behavior (coacervate). Following their experimentally reported work, here we report microsecond all-atomistic molecular dynamic simulations to confirm the effect of hydrophobicity on complexation in the same six polyelectrolyte systems. We simulate the interaction between the oppositely charged peptides for all six systems in explicit water with no additional salt and observe spontaneous complexation in all six simulations. We characterize the extent of interaction between the peptides in terms of hydrogen bonding and find agreement with the results of the original study of Tabendeh et al. We also further characterize the underlying peptide chain conformations using principal component analysis in the coacervate phase. We show that the minimum energy structure is modulated by the underlying sequence. These methods show a high potential to screen peptide conformation of intrinsically disordered peptides that form a high-density liquid phase in the phase-separated state.

The polyelectrolyte community has a long history of investigating how sequence affects the macroscopic phase behavior of these PECs. Models to describe the LLPS of intrinsically disordered peptides have strong underpinnings in polymer solution theory⁹. The phase behavior of complex coacervates that are driven by oppositely charged macromolecules can be predicted with classic Voorn-Overbeek theory¹⁰, polymer field theories that include fluctuations such as the Random Phase Approximation (RPA)¹¹, self-consistent field theory (SCFT)¹², and polymer reference interaction site model (PRISM)¹³ as thoroughly reviewed by *Sing et al.*¹⁴ Coarse-grained models such as the Restricted Primitive Model (RPM) represent the charged groups as hard spheres with explicit electrostatics have shown that shifting charge spacing can modulate the phase diagram¹⁵. Indeed, these models predict design rules for the critical point and critical density of these mixtures dependent on the degree and patterning of the hydrophobicity of these peptides¹⁶. While these theoretical tools describe the phase behavior, building atomistic detail into these models remains challenging.

There is a critical need to build atomistic chemical detail into more coarse-grained models and force fields. Sequence-specific models have demonstrated the potential of theoretical approaches to predict qualitative changes in the phase behavior based on specific amino acid residues¹⁷. Molecularly specific coarse-grained models such as the MARTINI model, specifically MARTINI 318, have also demonstrated that lower resolution models can predict/describe salt-dependent phase behavior for oppositely charged polypeptides. The potential of sequence-specific models, such as the MARTINI model, to predict LLPS for subtle differences in positioning and sequence for short peptides containing amino acids such as lysine, arginine, and tyrosine is an active area of interest. For example, additional models for intrinsically disordered peptides include work by Mittal et al. 17-19, Collepardo-Guevara et al. 20, Lindorff-Larson et al. 21, and more 22. While numerous coarse-grained simulations of liquid-liquid phase separation of intrinsically disordered peptides have been reported, there are comparably fewer studies of liquid phase separation with force fields that capture atomistic detail of peptides that exhibit LLPS at long time-scales¹⁹. While the role of chirality on the conformation of individual peptides has proven to be a determining factor in chain secondary structure^{7b, 23}. Here, we explore the initial stage of complexation for model peptide sequences that are oppositely charged and have alternating chirality within the chain using long-time atomistic molecular dynamics simulations. The computational investigations reported herein set the groundwork for further computational studies to explore the complex interplay between chirality and chain structure and how this is modulated by specific and directional

interactions with neighboring chains for these model peptides that form condensates.

H O DLYS H O

Figure 1. Schematic representation of the twelve peptide patterns. A single peptide system includes a combination of a positively (Lysine containing) and a negatively charged (Glutamate containing) peptide sequence. The top two models represent the first-generation pattern (equal charge density) while the bottom two models represent the second-generation pattern (double charge density). The **X** represents a variable residue which can be either Glycine, Alanine or Leucine. Oppositely charged peptides within a given system contain the same variable residue. The '**D** 'character indicates that the labeled residue is of D-chirality. All peptides are of alternating chirality, beginning with a D-chiral charged residue (DLYS or DGLU) and contain 30 residues (D-chiral, L-chiral)₁₅.

METHODS

Here, we report on all atomistic molecular dynamics simulations of the same six polyelectrolyte systems experimentally characterized by *Tabandeh et al*. These six model systems are built from twelve different peptide patterns (**Fig. 1**). Six of these peptide sequences correspond to the polycationic peptide (Lysine-containing) of a single system, while the other six sequences represent the polyanionic peptide (Glutamate-containing) of a single system. The hydrophobicity of a given peptide is modulated by one of three possible residues (Glycine, Alanine, and Leucine).

Three of the six peptide patterns for a given charge have a 1:1 ratio of charged residues to neutral residues, where the peptide alternates between charged and uncharged residues. The other three peptide patterns for a given charge have a 2:1 ratio of charged residues to neutral residues, where the peptide alternates between two charged residues and one neutral residue. These two groups of systems containing either single or double charge density are referred to as "first generation" and "second generation," respectively. All twelve peptide sequences contain 30 residues and are of alternating chirality, where the first residue is D-chiral as shown in Table S1.

8

9

10

11

12

13

14

1516

17

18

19

20

21

22

23

24

25

26

27

28

29

30

1

2

3

4

5

6

7

SIMULATION DETAILS

Singly Paired Peptide Systems

The initial coordinate files for all six peptide systems were built using the Discovery Studio Visualization tool²⁴, where the oppositely charged peptides of a single system are fully extended and positioned perpendicular to each other. These initial coordinates were solvated in an ion-free water box and prepared as an NPT ensemble for simulations using AMBER18²⁵ using CHARMM-GUI²⁶. Approximately 80,000 water molecules are needed to effectively solvate all six peptide structures. The six systems used the CHARMM36m²⁷ force field for peptides with the TIP3P water model. The CHARMM36m force field includes parameters for D-chiral amino acids. These solvated systems were minimized using the Steepest descent algorithm for 2500 steps followed by the conjugate gradient algorithm for an additional 2500 steps with a positional harmonic constraint applied to the peptides, as implemented in AMBER18. Subsequently, the systems were equilibrated in a two-step process while employing cartesian harmonic restraints on the peptide to preserve the orientation of the oppositely charged peptides for the production runs. The first equilibration step consisted of heating the entire system to a target temperature of 303.15 K from an initial temperature of 0 K over 1.0 ns. The second step employs constant pressure dynamics using an average pressure of 1.0 atm over 4.0 ns. Hydrogen bonds were constrained using the SHAKE algorithm²⁸. After equilibration, positional restraints were removed from the peptides and the systems were simulated for 0.2 µs. The collapsed conformations of the second-generation peptides were collected and resolvated to reduce the amount of water in the box for the remaining 0.8 µs. The temperature and pressure were controlled using the Langevin piston Nosé-Hoover method²⁹ with a damping coefficient of 1.0 ps⁻¹ and the MC barostat with a target external pressure of 1.0

atm. Electrostatics were handled using the Particle Mesh Ewald (PME)³⁰ method with a cut-off of 12 Å. These systems were simulated on local machines using 4 CPUs and 4 GPUs, achieving an average performance of 26 ns/days for the initial 0.2 μ s while the remaining 0.8 μ s achieved an average performance of approximately 200 ns/day. Trajectory sampling was done at every 10⁶ steps (2*10⁶ ps), resulting in 500 total snapshots representing 1 μ s. Analyses were done on the later 0.8 μ s portion. System sizes and simulation parameters are summarized in **Tables S1** and **S2** in the supplementary information.

7 8

9

10

11

12

13

14

15

16

17

18

19

20

21

22

23

24

25

26

27

28

29

1 2

3

4

5

6

Droplet Systems

Collecting the final collapsed structures of the positively and negatively charged strands from each of the six singly paired simulations, six new droplet configurations were constructed by randomly distributing these collapsed strands within a 189 Å³ box using Packmol³¹. For each configuration, twenty positively and twenty negatively charged strands were placed within a single box to produce six independent systems, each containing forty charged peptides in total (~10mM). The TIP3P water model and CHARMM36m force field were used²⁷. To prepare these configurations for simulations using GROMACS³², solvation and parameterization were done using the web tool, CHARMM-GUI^{26, 33}. Approximately 210,000 water molecules are needed to solvate these droplet systems. All six systems were minimized for 5,000 steps using the steepest descent algorithm, as implemented in GROMACS³⁴, with a force tolerance of 1000 kJ mol⁻¹ nm. During minimization, hydrogen bonds were constrained using the LINCS algorithm³⁵. After minimization, the systems were subjected to a one-step equilibration process which consisted of heating the systems to the target temperature of 303.15 K from an initial temperature of 0 K over 1.25 ps using an NVT ensemble with the Nose-Hoover Thermostat³⁶. After confirming that the systems were both thermally and energetically stable, the systems were simulated for 1.0 µs. Here, the Parrinello-Rahman barostat³⁷, with a pressure coupling time constant of 5.0 ps, is used to maintain constant pressure during the simulation. The Particle Mesh Ewald (PME)³⁰ method was used to handle electrostatics with a cut-off of 12.0 Å. Trajectory sampling was done at every 10⁵ steps (2*10⁵ ps), resulting in 5000 total snapshots representing 1 µs. Analyses were done on the later 0.6 µs portion. A summary of these simulation parameters can be found in **Tables S1** and S3 in the supplementary information.

30

31

ANALYSIS

Here we calculate various structural properties of the peptide chains. The radius of gyration for a peptide is defined as the distribution of its mass around its axis of rotation and is computed as the root mean square distance of each atom from the center of mass of the peptide. Radius of Gyration, R_g , such that $R_g^2 = (\sum_{i=1}^n m_i (r_i - r_c)^2) / (\sum_{i=1}^n m_i)$, values for an individual peptide are calculated for each frame of the trajectories. Here, m_i and r_c represent the mass of the ith atom, the position of the ith atom and the position of the center of mass of the peptide, respectively. Backbone hydrogen bonds are determined using the "hbonds" command from the Cpptraj package. Specifying a cutoff distance and angle, a hydrogen bond is determined to have occurred between an acceptor atom (F, O, and N atoms) and a donor atom (a hydrogen bonded to either F, O, and N atoms) if their distance and angle fall within 3.0 Å and 45°, respectively. Hydrogen bonds formed between the backbone atoms of the same peptide are categorized as intramolecular, while hydrogen bonds formed between the backbone atoms of separate peptides are characterized as intermolecular. To analyze the secondary structure content of a trajectory, a secondary structure type is assigned to each residue for each frame. These assignments were determined using the "secstruct" command from Cpptraj which uses the DSSP algorithm of Kabsch and Sander³⁸ to assign one of eight possible secondary structure types based on the position of the backbone amide and carbonyl groups. Here, secondary structures are determined over the backbone atoms of all residues. Principal component analysis (PCA) is a popular dimensionality reduction technique that can be used to both study and visualize a high-dimensional dataset. The goal of this technique is to find the best subspace representation for a set of datapoints. PCA calculations are further described in the supporting information. Highly populated regions of PCA space are believed to represent low-energy backbone conformations. These low energy conformations are then compared between the six different systems. Backbone ϕ and ψ angles of the peptides are calculated using the "multidihedral" command of the Cpptraj package from AmberTools20. The output was adjusted so that each row contained a single (ϕ, ψ) angle pair for each residue in a given frame. These values were then plotted as 2D histograms. The free energy for each bin is calculated using the same formula in PCA energy maps. All analyses were done using a combination of tools from the Cpptraj package of AmberTools20³⁹, VMD⁴⁰ and MDAnalysis⁴¹. Plots were generated using the matplotlib python package⁴².

1

2

3

4

5

6

7

8

9

10

11

12

13

14

15

16

17

18

19

20

21

22

23

24

25

26

27

28

Fourier Transform Infrared Spectroscopy

To experimentally measure the secondary structure of the peptide-based PECs we used attenuated total reflection Fourier transform infrared spectroscopy (ATR-FTIR) using a PerkinElmer Spectrum 100. PECS were prepared in D₂0, by mixing oppositely charged polypeptides at a charged monomer concentration of 100 mM and an equal charge ratio. After mixing, the PECS were centrifuged for 15 minutes at 10,000 rpm to separate the complex phase from the supernatant. Subsequently, 50 scans were run on the complex phase from 650 cm⁻¹ to 4000 cm⁻¹ at a resolution of 4 cm⁻¹. An air background scan was taken before each measurement and subtracted from the final spectrum. In addition, a D₂0 spectrum was taken and subtracted from the PEC measurements. The amide I spectral region containing the carbonyl stretching vibration was analyzed via deconvolution using the Gauss function in Origin software. Additional details are available in *Tabandeh et al.*⁸

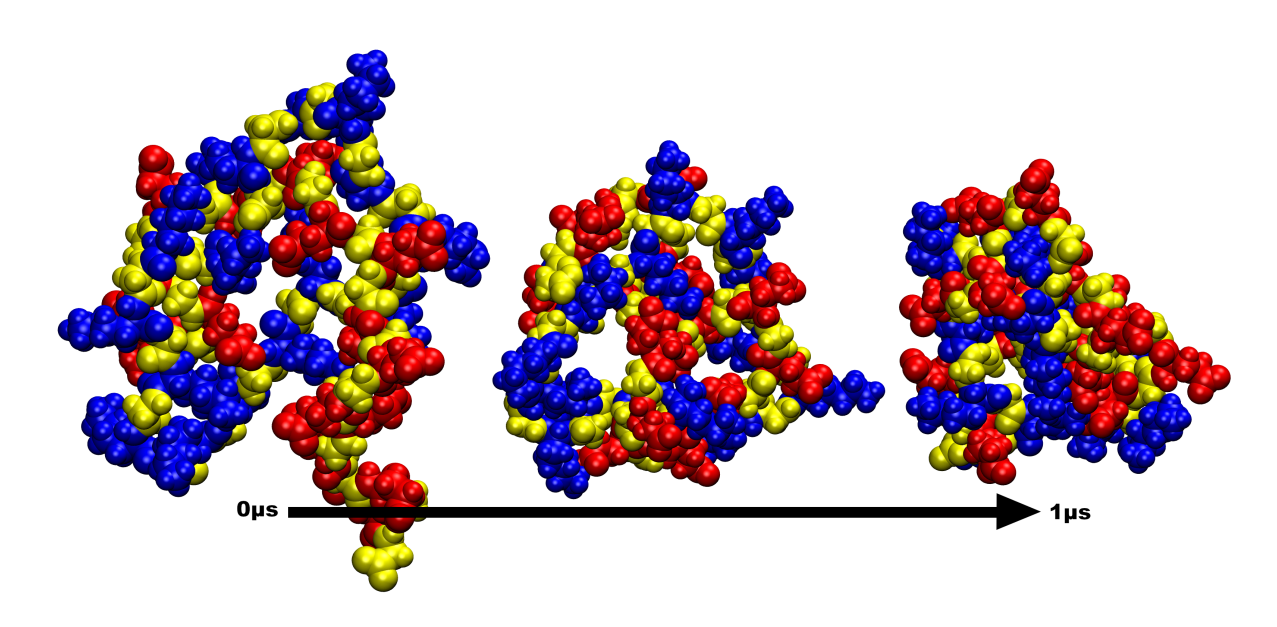


Figure 2. Snapshots of $(kG)_{15}+(eG)_{15}$ all atom system over 1 μ s. The two oppositely charged peptides are shown in Van der Waals representation and residues are colored by identity (Lys=blues, Glu=res, Gly=yellow). Surrounding water not shown.

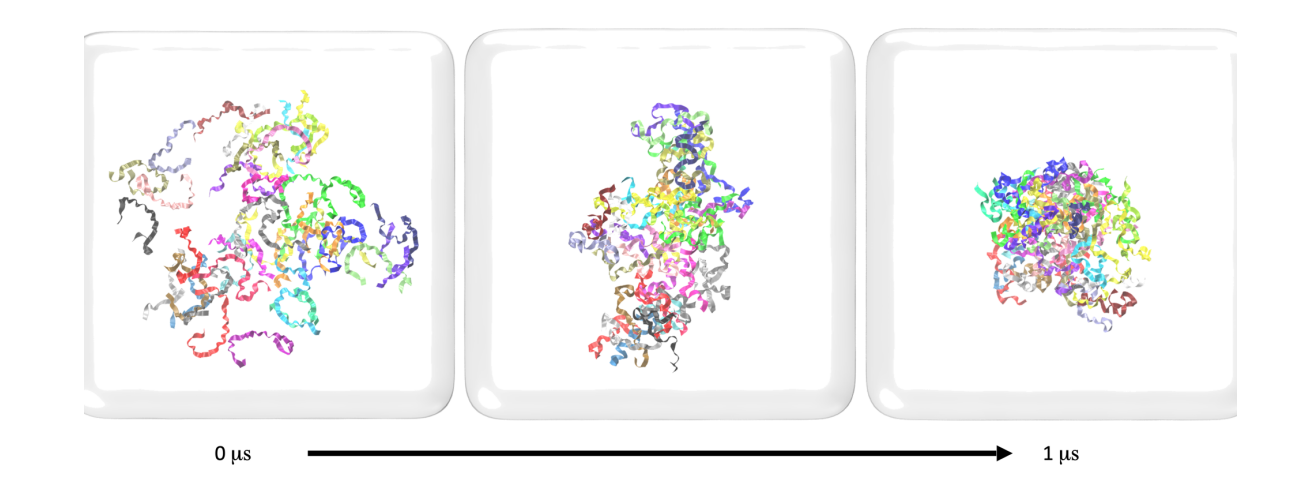


Figure 3. Time progression of p(kKlKkL)+p(eElEeL) system over 1 μs . The charged peptides are shown in ribbon representation and are colored by peptide identity.

RESULTS AND DISCUSSION

1. Simulation Overview

Exploring the role of hydrophobicity on the complexation of oppositely charged peptides, we aim to recapitulate the findings of the work done by *Tabandeh et al.* in the context of microsecond long all-atomistic molecular dynamic simulations. To this end, we start by first simulating the same six peptide systems as just single pairs of oppositely charged peptides within a salt-free water box. In these initial simulations, we observed the development of a collapsed dimer complex evolved from the formation of salt bridges, between the lysine and glutamate residues of the oppositely charged peptides, and intramolecular hydrogen bonds between the backbone atoms. This progression is showcased in **Fig. 2**, which displays three sequential snapshots of the p(kG)+p(eG) system over its 1 µs trajectory. Analyzing these simple systems, we found sensible trends in hydrogen bonding, radius of gyration (R_g) and secondary structure fractions which support the experimental findings of the original study.

Extending this study, we next simulated the aggregate behavior of these peptides using 1 µs simulations of six new 'droplet' systems, each having peptide concentrations at 10 mM (details on the preparation of these systems can be found in the methods section and in **Table 1** of the supplementary information). For these new systems, we observe the immediate diffusion of the oppositely charged peptides to form a single droplet phase within the first half of the trajectory (**Fig. 3**). These final droplets are shown in **Fig. S7**. Given the trends observed for the singly paired

systems, we speculated whether the same trends would persist in the droplet systems. To test this idea, we applied the same four analyses done on the singly paired systems towards these new droplet systems to directly compare the results. The main results for both the singly paired and droplet systems are summarized and discussed in the subsequent sections.

1 2

1.1. Distance Between Centers of Mass Singly Paired Peptides

To monitor this complexation process, the distance between the center of mass for each peptide is collected over time, as shown in **Fig. S1**. We observe that this calculated distance decreases rapidly within the first few frames but fluctuates for the remainder of the trajectory. Interestingly, the Ala-containing peptides of the second generation showcase larger fluctuations in distance, producing a significantly higher average distance at around 6.5 Å (**Fig. S2**). This suggests that a more complex method, in addition to regular MD, may be required to relax the system. Despite this anomaly, the other five systems showcase similar average distances within 3.5 Å and 4.5 Å. Overall, visual inspection of these trajectories shows that all six systems can form a stable complex early in the simulation and maintain this complex for the remainder of the trajectory. While no clear trend can be drawn from the distance between the peptide's centers of mass, we move on to explore how the variable residue can affect the conformation of its associated peptide.

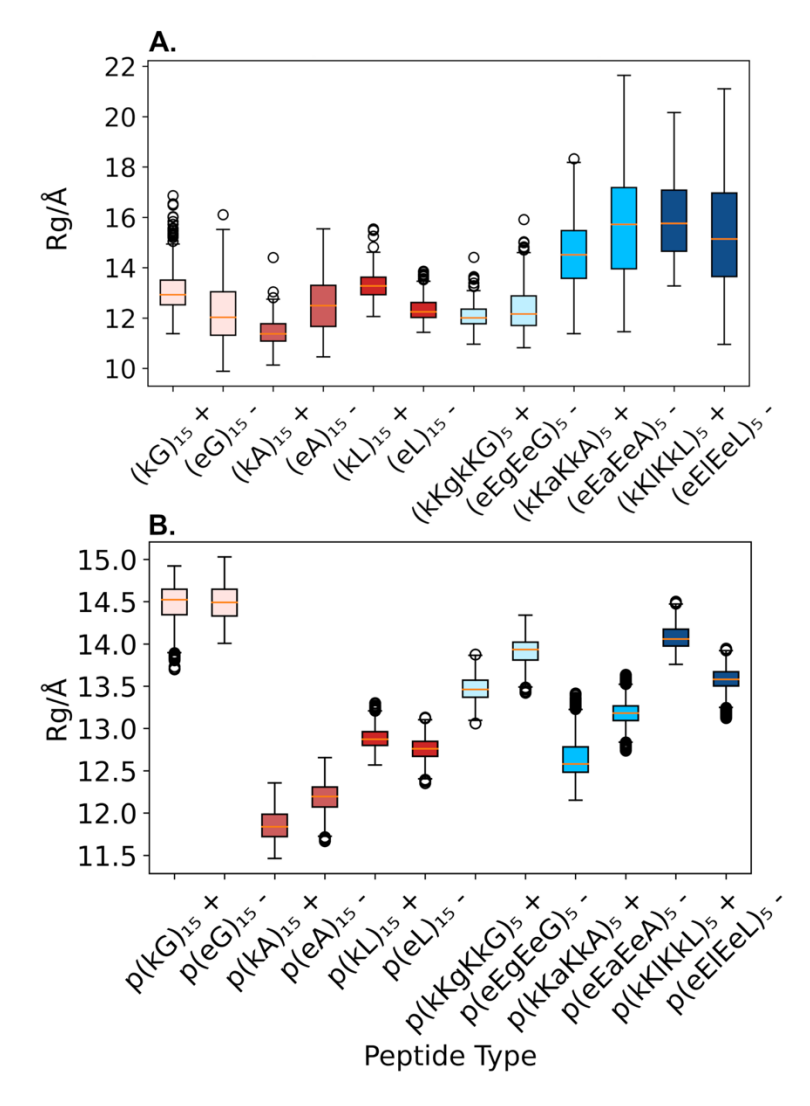


Figure 4. Variation in calculated radius of gyration values. **A.** Box and whisker plots of calculated R_g for a single peptide within a single paired system. Systems of equal charge density are shown in shades of red while systems containing double charge density are shown in shades of blue. **B.** Variation in calculated average R_g for droplet systems. Each box plot showcases the variation in the calculated average R_g values for a single peptide type (ie. All positive peptides (left) or all negative peptides (right) in a single water box). Systems of equal charge density are shown in shades of red while systems containing double charge density are shown in shades of blue.

1.2. Radius of Gyration

To characterize the extent of collapse of the charged peptides within each system, we measure the radius of gyration (R_g) for individual peptides over time (**Fig. S3, S8**) and compare these values using box plots as shown in **Fig. 4**. The R_g of a peptide measures the distribution of atoms from its axis of rotation and enables simple quantification of the general structure of the complexed peptides where decreasing R_g values are associated with peptide collapse and greater compaction.

To simplify the comparison between the droplet systems, the average R_g is calculated over each of the 20 identical peptides for each droplet system to form a single time series for the positively and negatively charged peptides (Fig. S8). These averages are then organized as box plots to compare the R_g distribution between the six droplet systems (**Fig. 4B**) and the six single systems (**Fig. 4A**). Raw histograms of the R_g values are also provided in the supplementary information (Fig. S10, S11). Using this method, we first note a smaller inter-quartile range for the droplet peptides, indicating that these peptides exhibit less conformational flexibility in a crowded environment, likely due to the combined effect of steric hindrance between neighboring peptides and the formation of salt bridges between multiple peptides. Surprisingly, the median R_g changes only slightly between the first-generation systems of the singly paired and droplet simulations. This may be an effect of averaging over identical peptides, as more extended Rg values from peptides at the surface of the droplet are offset by more collapsed R_g values from buried peptides. We next note significantly higher average R_g values for alanine and leucine-based peptides of the second-generation when compared to their first-generation counterparts (i.e., p(kX)₁₅ vs. p(kKxKkX)₅) for both the single and droplet simulations. This could be attributed to the higher charge density of the second-generation peptides, which may inhibit their ability to collapse on themselves due to the combined effect of mutual charge repulsion and the formation of persistent salt bridges between the separate peptides, which imparts local rigidity 43 . However, the Glycine-based peptides exhibit $R_{\rm g}$ values that diverge from this expectation, producing similar R_g values between both generations in the single peptide case and significantly higher R_g values in the packed case. Given Glycine's small size, we speculate that this residue imparts minimal obstruction to hydrogen bond formation, as well as a smaller hydrophobic tendency for the chain to collapse.

Originally, we had expected that $R_{\rm g}$ would increase with the hydrophobicity and charge density of the peptide pattern to reflect the extent of hydrogen bonding. In the singly paired simulation, the calculated $R_{\rm g}$ does not clearly reflect this specific trend, showing overlapping distributions which make it hard to discern a clear trend in hydrophobicity. In the droplet simulations, the $R_{\rm g}$ values are more localized around a single value but don't reflect this trend. However, we do observe a consistent trend between the two generations where the Ala-based peptides show either low or comparable $R_{\rm g}$ values to the Leu-based peptides in both the droplet and single simulations.

2930

31

1

2

3

4

5

6

7

8

9

10

11

12

13

14

15

16

17

18

19

20

21

22

23

24

25

26

27

28

1.3. Backbone Hydrogen Bonding

The main interaction stabilizing PECs is electrostatic, but it well known that secondary interactions such as backbone hydrogen bonds are important factors in determining PEC stability^{1b}. Given the ability of peptides to form backbone hydrogen bonds, these twelve peptide patterns were originally engineered to probe the role of hydrophobicity on the final physical properties of the formed PEC, with a heavy inclination towards modulating their ability to form backbone hydrogen bonds. To study this effect, we next calculate the time-averaged hydrogen bond counts for identical peptides over all six systems (Fig. S12) and organize these results as bar plots (Fig. 5) to understand how the variable amino acid affects the engagement of these charged peptides in backbone hydrogen bonding. Here we observe two distinct trends with respect to the length of the variable amino acid and the charge density of the peptide. The first trend involves a clear increase in the average count of formed intramolecular hydrogen bonds with respect to the length of the variable side chain in the first generation but a decrease in the second generation (Fig. 5A, C). This trend in emphasized through hydrogen bond contact maps of the singly paired systems in Fig. S4 where higher intramolecular hydrogen bond fractions are observed for the charged strands of the firstgeneration sequences. This could suggest that longer side chains within the first generation help to stabilize the collapsed peptide, as suggested by smaller distributions of R_g as previously shown in Fig. 3A. We see the opposite trend in the second generation where the average intramolecular hydrogen bond count seems to decrease with increasing side chain length. This may offer an explanation to the observed shift to larger R_g values for the second-generation systems.

1

2

3

4

5

6

7

8

9

10

11

12

13

14

15

16

17

18

19

20

21

22

23

24

25

26

27

28

The second trend is a clear decrease in the number of intermolecular hydrogen bonds with respect to the variable side chain length for both generations. In the singly paired systems, we find higher intermolecular hydrogen bond counts in the second-generation systems which is expected from an increased electrostatic repulsion and stretching of the chains. Surprisingly, we see that the first-generation systems show higher average intermolecular hydrogen bond counts despite the double charge density of the second-generation systems. We hypothesize that the higher charge density of these peptides decreases the overall probability of intermolecular hydrogen bonding in the droplet systems due to the possibility of identically charged peptides to neighbor each other within the local structure of the droplet, an effect absent in the singly paired chains.

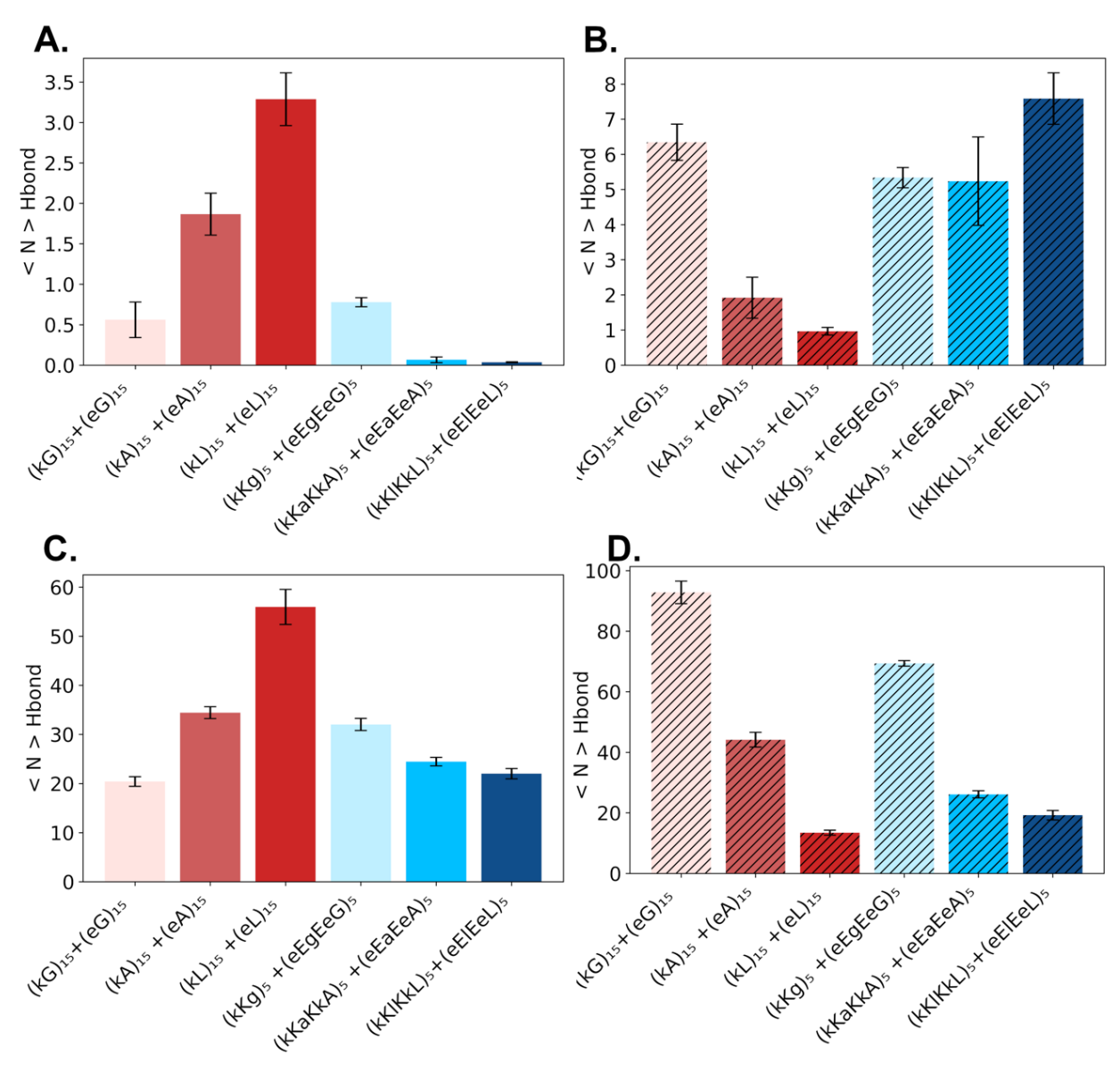


Figure 5. Calculated average hydrogen bond counts. **A.** Average intramolecular hydrogen bond counts for the singly paired systems. **B.** Average intermolecular hydrogen bond counts for the single paired systems. Both calculations for the singly paired systems were taken over the last $0.8 \, \mu s$. **C.** Average intramolecular hydrogen bond counts for the droplet systems. **D.** Average intermolecular hydrogen bond counts for droplet systems. Both calculations for the droplet systems were taken over the last $0.6 \, \mu s$. Systems containing equal charge density are colored in red while systems containing double charge density are colored in blue. Averages and errors were calculated using block averaging.

1.4. Secondary Structure Propensity

Peptides have the unique ability to form regular secondary structure motifs facilitated by backbone hydrogen bonding. The district trends found in the hydrogen bonding analyses would suggest distinct trends in secondary structures. To confirm this, we calculated the secondary structure fractions for each system over the equilibrated subset of the microsecond trajectory and directly compare these results with the FTIR results from the work of *Tabandeh et al* (**Fig. 6**). The fraction values used here are derived from the secondary structure classification of individual residues using the DSSP algorithm³⁸. Here, we consider the eight reported structure types in terms of three general structure type: loops, strands, and helices. The loop type incorporates random coils ("None"), "Bends" and "Turns," representing residues not engaged in strict secondary structure patterns such as helices or β -sheets. The strand type incorporates Extended and Bridge assignments, representing residues that are classified to be engaged in either parallel or antiparallel β -sheet structures (the DSSP algorithm classifies β -sheet structures as stretched of smaller β -bridge structures). The helix type combines the "3-10", "Alpha" and "Pi" assignments to represent residues engaged in 3-10 helices, α -helices, and π -helices respectively.

The calculated secondary structure fractions for the single and droplet systems are shown in **Fig. 6A**, **B**. Here, we observe that the prominent secondary structure types are loop-like with minimal engagement in ordered structures (helix and strand types). Given the timescale needed to observe amyloid structure in unbiased MD simulations, this is to be expected. However, we do observe a non-negligible fraction (>10%) of residues participating in strand structures during the 1 μ s trajectory. While these calculated β -sheet fractions are not directly comparable with the experimental FTIR results, we still observe a similar trend of decreasing ordered secondary structure content with increasing variable hydrophobic residue length. In the single systems, explicit random coil fractions appear to increase with increasing hydrophobicity and charge fraction starting from p(kA)+p(eA). Similarly, we observe an increase in loop propensity with increasing peptide hydrophobicity for the droplet systems. Overall, the calculated secondary structure fractions appear to be qualitatively aligned with the FTIR results if we generalize the eight specific secondary structure types into just three types (i.e. Loops, Helices and Strands).

To further characterize the conformation of the peptide complexes, we next calculated the distribution of backbone dihedral angles for the individual peptides over the same equilibrated time span (0.8 μ s and 0.6 μ s) and plot these distributions as Ramachandran (ϕ/ψ) plots for comparison (**Fig. 7, S5, S6, S13,** and **S14**). These plots can be used to visualize energetically feasible

by considering the area of disallowed regions. Here, we use these plots to compare the effect of the variable residue of the peptide backbone by considering only the torsion angles of every sixth residue along the Lysine-containing strand of a given system (**Fig. 7**). This set of residues corresponds to a variable residue group neighbored by two D-chiral Lysine (k-X-k) for all twelve patterns, resulting in 4 and 80 dihedral angle pairs for the single and droplet systems respectively. Ramachandran plots for the negatively charged strands are not shown to avoid redundancy.

We first considered the effect of the variable residue on torsion angle distributions for the singly paired systems in Fig. 7A-F. Here, we observed a shift in torsion angle distributions with variable residue. In **Fig. 7A**, we can see that the Glycine residues take on dihedral angles at four small clusters with (φ, ψ) values falling within the expected allowed regions for glycine residues in a folded protein⁴⁴. Two of these clusters are located at $\varphi > 0$ and do not correspond to regular secondary structure patterns, emphasizing the conformational flexibility of the Glycine residue. Similarly, the Ramachandran plots for Alanine and Leucine residues (Fig. 7B, C) shows only a single main large cluster within (φ, ψ) values commonly associated with distinct secondary structure patterns that are subtypes of beta sheets and helices⁴⁴. For Alanine, its main cluster can be roughly boxed within (-180 $< \varphi <$ -60) and (100 $< \psi <$ 180). Dihedral angles falling within this box correspond to several secondary structure types: Parallel β-pleated sheet, Antiparallel βpleated sheet, Collagen and Polyproline II helices 44. Similarly, Leucine's main cluster falls within $(-180 < \varphi < -60)$ and $(-90 < \psi < 25)$. These dihedral angles correspond to either Right-handed 3-10 helices, Right-handed π helices, and Left-handed α helices⁴⁴. Due to the largely solvent-exposed backbones, we expect that these peptides are engaged in transient structures, explaining their apparent conformational diversity.

Interestingly, the dihedral distributions are significantly different for the same residue pattern between the two generations. For example, **Fig. 7A** shows the dihedral distribution of four separate Glycine residues along the chain defined by the first-generation sequence (kG)₁₅, while **Fig. 7D** shows the dihedral distribution of four separate Glycine residues along the chain defined by the corresponding second-generation sequence (kKgKkG)₅. Despite measuring the dihedral angle of four separate Glycine residues, each between two D-chiral Lysine's, these two plots show different dihedral distributions. This would suggest that the backbone conformation of a given residue is influenced by factors beyond its immediate neighboring residues. We hypothesize that

both the differences along the entire sequence of a single chain and the effect of complexation between both chains may explain the observed difference in dihedral distribution for the same three residue pattern between both generations.

We next considered whether the same shifts would be observed in the droplet simulations. Due to the larger number of residues being measured and the higher sampling frequency of these simulations, the resulting plots show larger variation in torsion angle values and are not directly comparable to the singly paired case. However, we still observe a shift in torsion angle distributions with variable residue identity (**Fig. 7G-L**). Further, highly populated torsion angles in the singly paired simulations appear to be conserved in the droplet simulations but are more pronounced for the reasons stated previously. For p(kG), we see four large clusters in each quadrant, overlapping with the clusters observed in the singly paired systems, displaying the conformational freedom of Glycine. For p(kA), heavy clusters are observed in the upper left quadrant, while the p(kL) are heavy in the lower left quadrant and upper left. For all six plots, we can see that this subset of 80 residues shows dihedral angle distributions in the upper left quadrant and the lower left quadrant, corresponding to β -sheet and right-handed helices. We note that the left-handed helix population decreases, and the right-handed helix content becomes more prevalent as the size of the hydrophobic group increases.

Overall, we observe characteristic dihedral distributions between all six systems. The difference between the generations is more subtle. Comparison of only a specific set of residues allows qualitative comparisons between the systems, where favorable dihedral angles appears to shift towards the right half of the Ramachandran plot with an increase in variable residue length, but does not allow us to connect secondary structure propensities of the systems. To this end, we also plot the dihedral distributions of all residues (**Fig. S13** and **Fig. S14**). Here, we can see both the conformations of both L-chiral and D-chiral residues. Observing these characteristic differences in dihedral angle distributions, we go on to explore whether we could also observe these different backbone conformations of the individual peptides in each of the six droplet systems by applying Principal Component Analysis (PCA) towards the atomic coordinates of the peptide backbone.

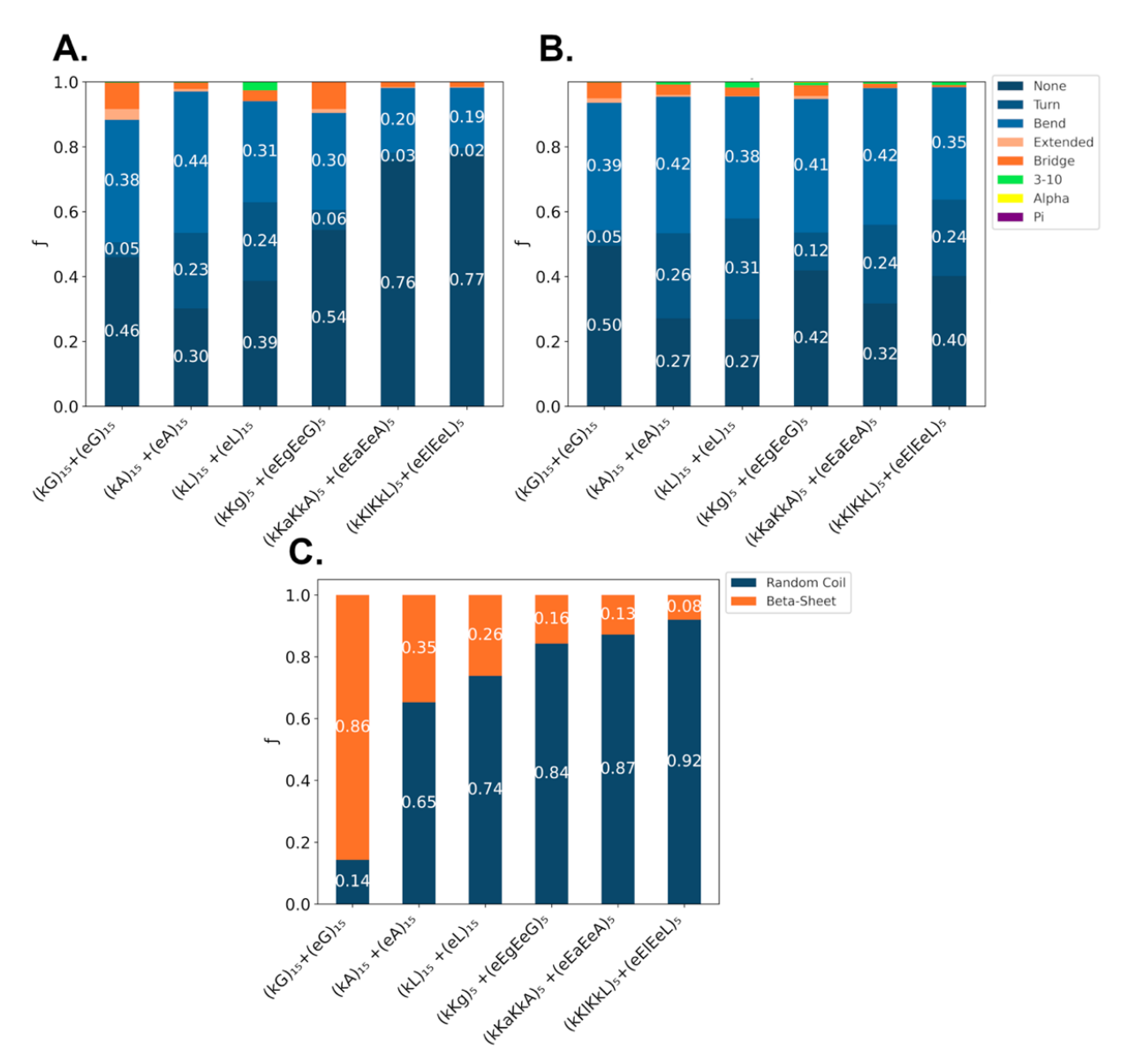


Figure 6. Calculated secondary structure fractions. **A.** Secondary structure fractions over all residues within a given singly paired systems (over the last 0.8 μs). Secondary structure assignments were determined using the DSSP algorithm, which reports eight possible structure types. Here, we interpret the eight structure types in terms of three general type: loops ("None", "Bends", "Turns"), strands ("Extended", "Bridge") and helices ("3-10", "Alpha", "Pi"). **B.** Calculated secondary structure fractions over all residues within each droplet system (over the last 0.6 μs). **C.** FTIR results of the PECs from Tabandeh et al. showing an increase in random coil structure with hydrophobicity for both first generation and second-generation sequence pairs. Also, random coil structure increases from the first generation to the second. PECs are formed at a concentration of 100 mM monomer charge in D_20 and centrifuged to separate the complex phase from the supernatant. ATR-FTIR is performed on the complex phase. The amide I region from 1600-1700 cm⁻¹ is analyzed via deconvolution to obtain the b-sheet and random coil fractions (f) presented in this figure.

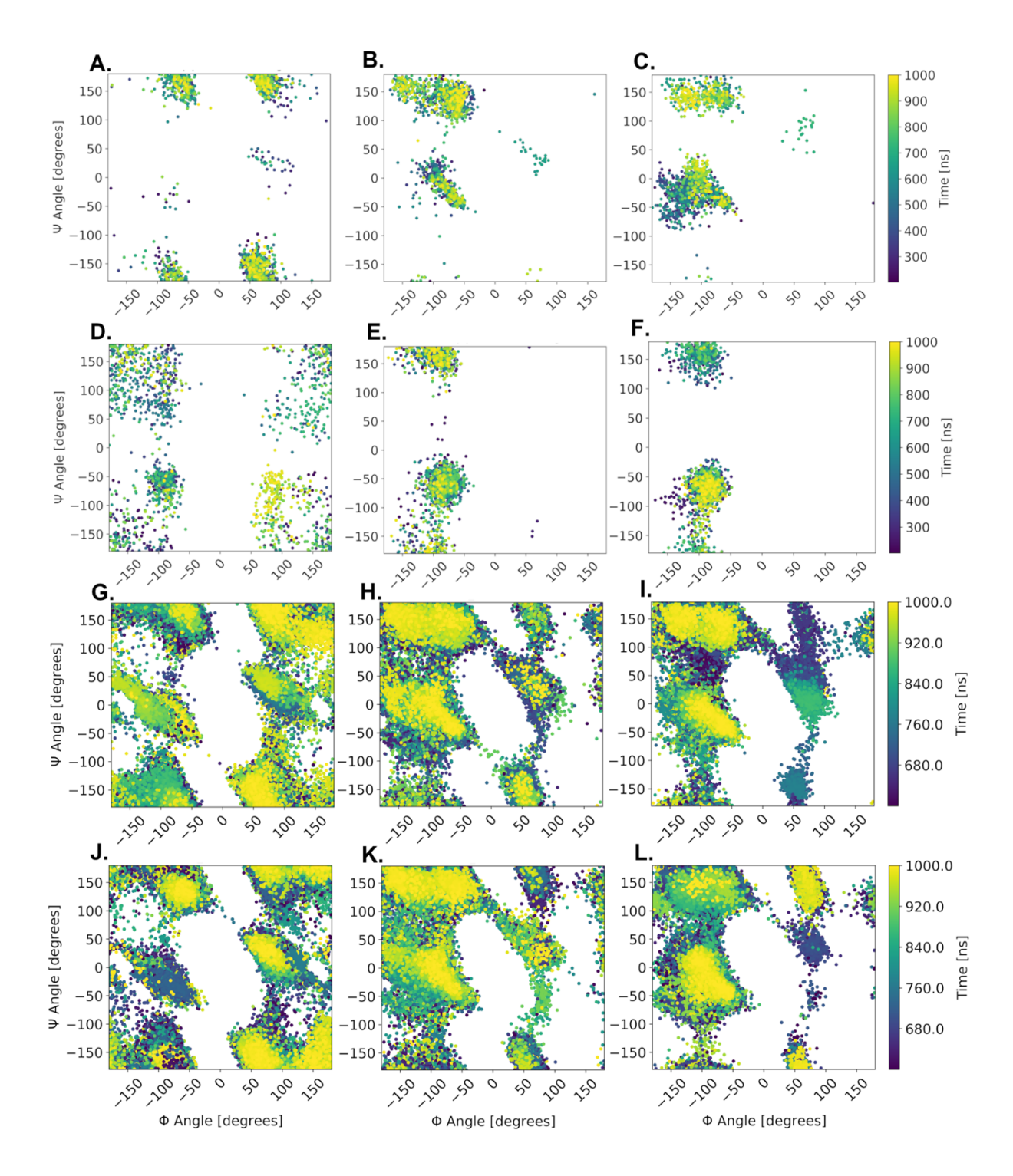


Figure 7. Dihedral Angle Variation. The top six plots (**A-F**) showcases the dihedral angle progression for the sixth residue of each positively charged strand within a single paired system. The bottom six plots (**G-L**) showcases the dihedral angle progression for the sixth residue of all 20 positively charged strands within a single droplet system. **A.** p(kG), **B.** p(kA), **C.** p(kL), **D.** p(kKgKkG), **E.** p(kKaKkA), **F.** p(kKlKkL), **G.** p(kG), **H.** p(kA), **I.** p(kL), **J.** p(kKgKkG), **K.** p(kKaKkA), **L.** p(kKlKkL). For all peptide patterns, the 6th residue is a variable amino acid adjacent to two D-chiral lysines (DL-X-DL).

2.5. Principal Component Analysis

PCA is a common dimensionality reduction technique used in statistics where the goal is to transform features of a dataset onto a lower dimensional space (PCA space) which captures the directions of maximum variance. The independent directions which define this lower dimensional space are referred to as "Principal Components" and they represent the directions of maximum variance within the original dataset. In the context of molecular dynamics, the coordinates of each atom in a trajectory can be projected onto this lower dimensional subspace where its principal components represent the largest uncorrelated motions of the trajectory dataset⁴⁵. Here, we use the PCA method to compress the individual peptide motions of the droplet trajectory into a series of "conformations" based on their projection onto only the first two principal components. These projections onto the calculated 2D-PCA space are then used to create contour plots colored by the calculated free energy. Fig. 8 shows the PCA space for the positively charged strands, and Fig. 9 shows the PCA space for the negatively charged strands. Each figure showcases the calculated free-energy landscape of identical peptides for each of the six systems and an example snapshot of a conformation whose projection lies in the lowest energy basin. Further details can be found in the methods section.

The six free energy landscapes contain multiple low energy basins for backbone coordinates that cluster together in PCA space, possibly indicating multiple stable conformations of the peptide backbone. Like the dihedral distributions, the Glycine-containing peptides appear to showcase higher conformation variability relative to the other systems, having coordinates that cover a larger region of PCA space. While it is difficult to make comparisons between separate PCA spaces, we can make comparisons between the conformations of the lowest energy regions. Inspecting these low energy conformations, we derive qualitative trends in the extent of backbone folding where the Glycine strands appear more extended while the Ala-based and Leu-based strands are more collapsed. To confirm this observation, intramolecular hydrogen bond contact maps, and average Rg are calculated over the original frames corresponding to these low energy conformations in PCA space (Fig. S15 and Fig. S16). The calculated Rg values do not follow the trend for hydrophobic side chain length. However, the second-generation Rg values indicate the chains are more extended. However, they appear to re-capture some of the same trends seen in

hydrogen bonding despite using only a fraction of the total frames. Ultimately, the derived conformations seem to highlight the previous trends seen and emphasize the key conformations of the backbones as an effect of the sequence pattern. We plan to further explore this method in highlighting the key differences in dynamics by comparing how these coordinates cluster in higher spaces.



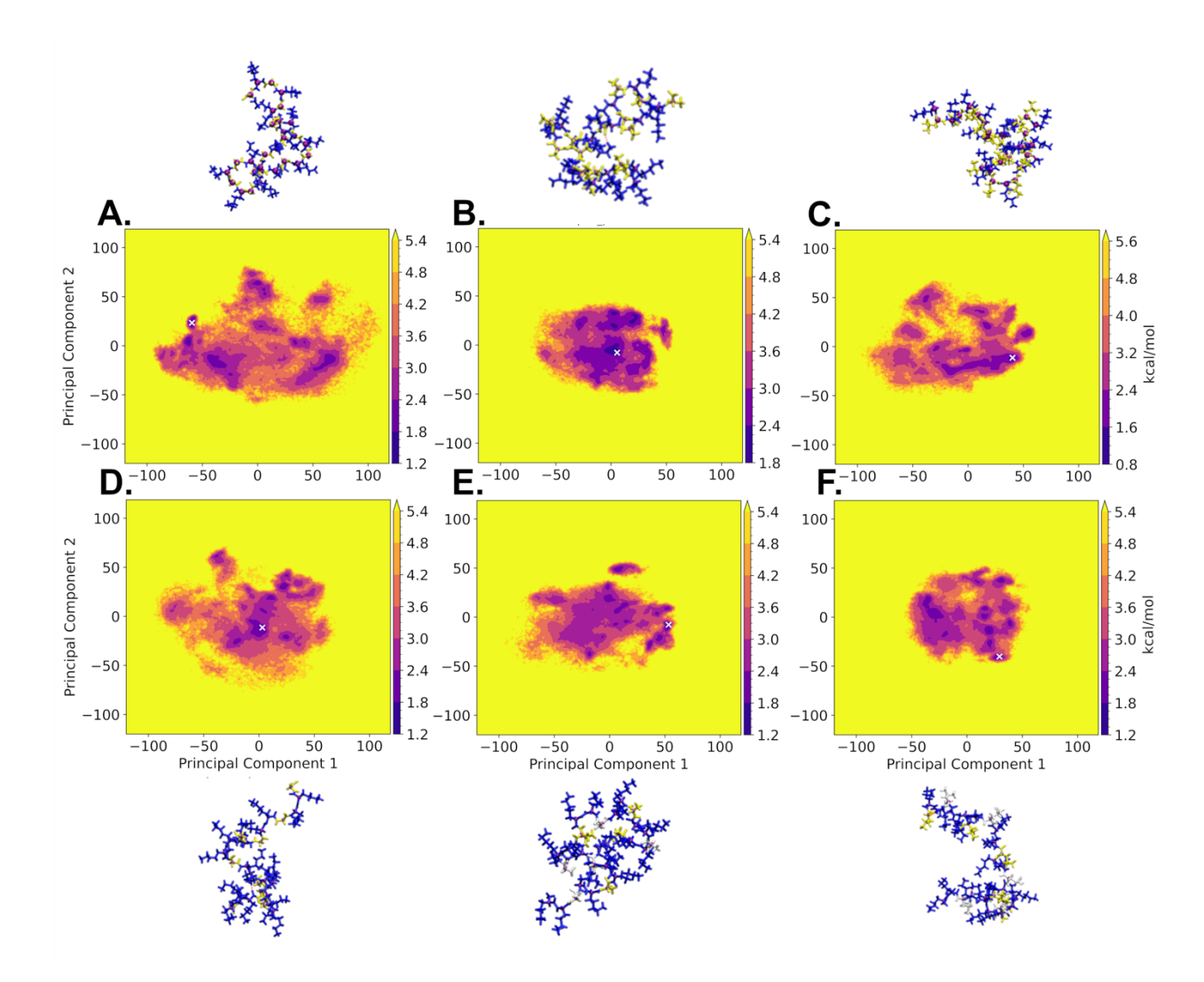


Figure 8. PCA analysis of all 20 positively charged strands within each packed peptide systems. **A.** $p(kG)_{15}$, **B.** $p(kG)_{15}$, **C.** $p(kL)_{15}$, **D.** $p(kKgKkG)_5$, **E.** $p(kKaKkA)_5$, **F.** $p(kKlKkL)_5$. Example conformations were taken from the bin with the lowest calculated energy (highlighted with a green dot) and are shown either above or below their corresponding energy map.

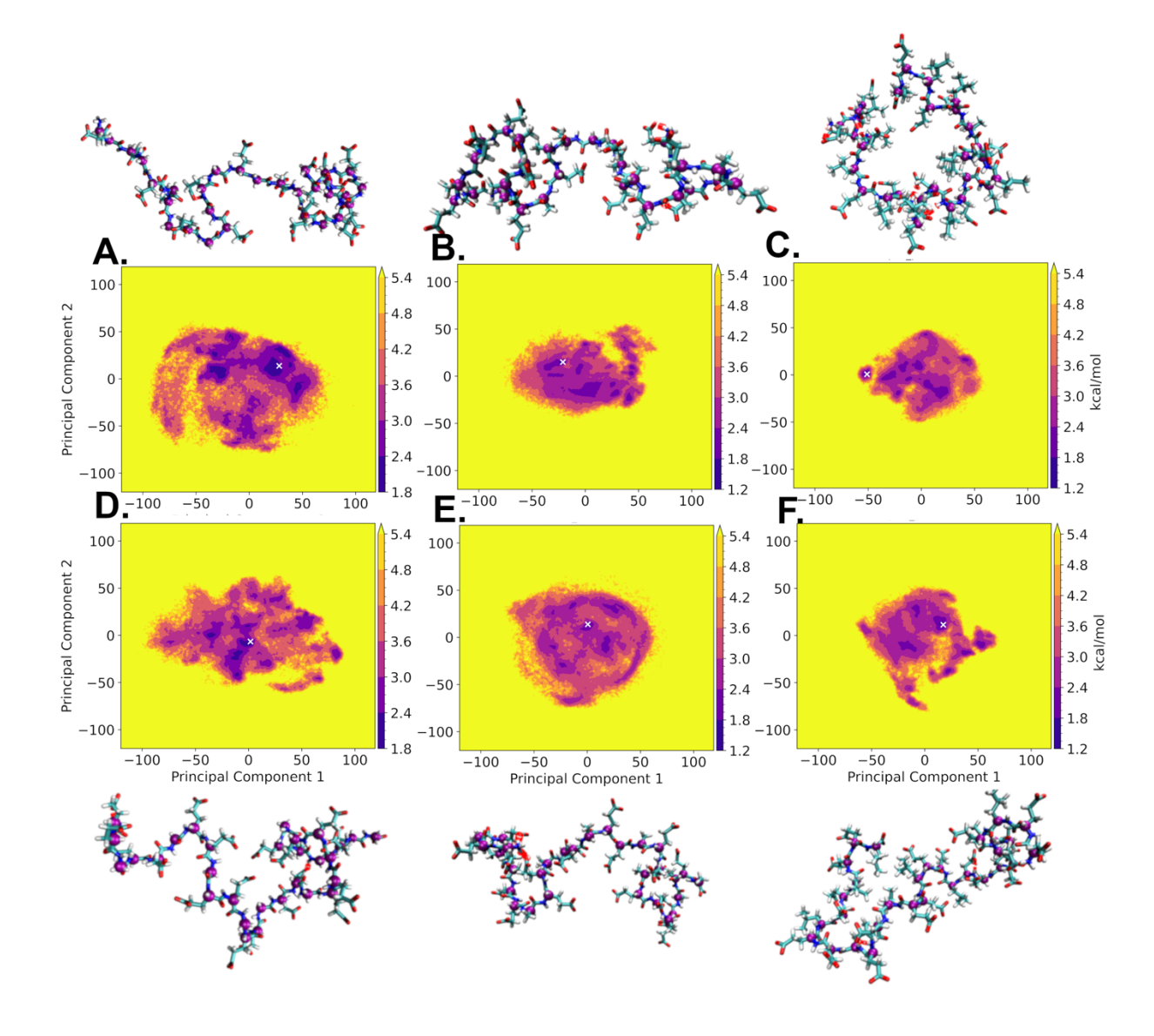


Figure 9. PCA analysis of all 20 negatively charged strands within each packed peptide systems. **A.** $p(eG)_{15}$, **B.** $p(eA)_{15}$, **C.** $p(eL)_{15}$, **D.** $p(eEgEeG)_5$, **E.** $p(eEaEeA)_5$, **F.** $p(eElEeL)_5$. Example conformations were taken from the frame of the reshaped trajectory corresponding to the bin with the lowest calculated energy (highlighted with a white X) and are shown either above or below their corresponding energy map.

CONCLUSION

2

- 4 Critical barriers toward realizing the detailed sequence-specific design of peptide-based
- 5 PECs includes a bottom up understanding of how the inclusion of hydrophobic side chains affects

the backbone structure and mobility of the peptides. Here we show that the size of the intercalated hydrophobic group within a peptide sequence of alternating chirality, previously observed to exhibit liquid-liquid phase separation, can modulate not only the intermolecular hydrogen bonding between strands, but also the underlying backbone conformation for neighboring residues. Thus, the size of the hydrophobic group can influence the overall secondary structure propensity of the sequence, with larger intercalated hydrophobic sidechains favoring decreasing β -sheet content. Decreasing β -sheet content in the higher density liquid phase should increase diffusion and modulate the local viscoelasticity. Such studies will give critical insight into the design of new peptide biomaterials from the sequence level up that can be used for diverse applications in bio-sensing, bio-mimetic, and bio-therapeutic materials.

Given the observed trends observed in only six sequences, we hypothesize that additional peptides of similar alternating structure would also showcase notable trends in R_g and secondary structure propensities. By varying charge, hydrophobicity, and 'blockiness' of a given peptide, we next plan to screen a set of strategically designed charged peptide sequences to characterize in more detail how neighboring amino acid sequences can shift single chain secondary structure. This approach of peptide screening has already been shown to be a viable method towards the rational design of self-assembled materials⁴⁶ and the prediction of structural ensembles⁴⁷. Further, this method has recently gained momentum due to the combined availability of powerful computing resources and machine learning methods. Regular molecular dynamics could lead to the coacervate droplets being stuck in a metastable state. Free energy approaches could be used to further relax the conformations of the peptides in the droplet⁴⁸. However, theoretical tools, such as free energy methods, to characterize the underlying molecular pathway based on peptide

- 1 chemistry can be further developed and refined. We are currently exploring the potential of ad-
- 2 vanced free energy methods in molecular dynamics such as metadynamics⁴⁹ to describe fluctua-
- 3 tions in peptide density and the formation of liquid droplets on the pathway to supramolecular
- 4 fibers⁵⁰. Overall, the trends observed here suggest an opportunity to rationalize the behavior of
- 5 charged peptides in the context of varying hydrophobicity from the sequence level up.

6

7

8

14

ASSOCIATED CONTENT

- 9 **Supporting Information.** Figures S1-S16 contain further structural and interaction data for the
- single and droplet peptide systems.

11 AUTHOR INFORMATION

12 Corresponding Author

sharon.loverde@csi.cuny.edu

Author Contributions

- 15 The manuscript was written through the contributions of all authors. All authors have approved
- the final version of the manuscript.

17 Funding Sources.

- Acknowledgments. S. M. L. acknowledges start-up funding received from College of Staten Is-
- 19 land and City University of New York. S. M. L. would also like to acknowledge NSF Grant DMR-
- 20 1750694 and NSF NRT grant DGE-2151945, and NIH NIGMS 1R15GM146228-01. We also
- 21 acknowledge support for the CUNY HPCC from NSF grant 2215760. We acknowledge support

- 1 from NSF ACCESS. T. R. would also like to acknowledge partial support from the Rosemary
- 2 O'Halloran scholarship, which supports female graduate students at CUNY College of Staten Is-
- 3 land in the Chemistry department. S.T. and L.L. would like to acknowledge support from the Na-
- 4 tional Science Foundation, Division of Materials Research, Award Number 2045454.

5 Bibliography

- 6 (1) (a) Wang, Q. F.; Schlenoff, J. B. The Polyelectrolyte Complex/Coacervate Continuum.
- 7 *Macromolecules* **2014**, 47 (9), 3108-16. DOI: 10.1021/ma500500q. (b) Perry, S. L.; Leon, L.;
- 8 Hoffmann, K. Q.; Kade, M. J.; Priftis, D.; Black, K. A.; Wong, D.; Klein, R. A.; Pierce, C. F.;
- 9 Margossian, K. O.; et al. Chirality-selected phase behaviour in ionic polypeptide complexes. *Nat.*
- 10 Commun. 2015, 6 (1), 6052. DOI: 10.1038/ncomms7052. (c) Pacalin, N. M.; Leon, L.; Tirrell,
- 11 M. Directing the phase behavior of polyelectrolyte complexes using chiral patterned peptides.
- 12 European Physical Journal: Special Topics **2016**, 225 (8-9), 1805-15. DOI:
- 13 10.1140/epjst/e2016-60149-6. (d) Vieregg, J. R.; Lueckheide, M.; Marciel, A. B.; Leon, L.;
- Bologna, A. J.; Rivera, J. R.; Tirrell, M. V. Oligonucleotide-Peptide Complexes: Phase Control
- by Hybridization. *Journal of the American Chemical Society* **2018**, *140* (5), 1632-8. DOI:
- 16 10.1021/jacs.7b03567. (e) Liu, Y. L.; Momani, B.; Winter, H. H.; Perry, S. L. Rheological
- 17 characterization of liquid-to-solid transitions in bulk polyelectrolyte complexes. *Soft Matter*
- 18 **2017**, 13 (40), 7332-40. DOI: 10.1039/c7sm01285c.
- 19 (2) (a) Hoffmann, K. Q.; Perry, S. L.; Leon, L.; Priftis, D.; Tirrell, M.; de Pablo, J. J. A
- 20 molecular view of the role of chirality in charge-driven polypeptide complexation. Soft Matter
- 21 **2015**, 11 (8), 1525-38. DOI: 10.1039/c4sm02336f. (b) Michaels, A. S. POLYELECTROLYTE
- 22 COMPLEXES. *Industrial and Engineering Chemistry* **1965**, *57* (10), 32-40. DOI:
- 23 10.1021/ie50670a007. (c) Chollakup, R.; Beck, J. B.; Dirnberger, K.; Tirrell, M.; Eisenbach, C.
- D. Polyelectrolyte Molecular Weight and Salt Effects on the Phase Behavior and Coacervation of
- 25 Aqueous Solutions of Poly(acrylic acid) Sodium Salt and Poly(allylamine) Hydrochloride.
- 26 Macromolecules **2013**, 46 (6), 2376-90. DOI: 10.1021/ma202172q. (d) Priftis, D.; Tirrell, M.
- 27 Phase behaviour and complex coacervation of aqueous polypeptide solutions. *Soft Matter* **2012**,
- 28 8 (36), 9396-405. DOI: 10.1039/c2sm25604e. (e) Cooper, C. L.; Dubin, P. L.; Kayitmazer, A.
- 29 B.; Turksen, S. Polyelectrolyte-protein complexes. Curr. Opin. Colloid Interface Sci. 2005, 10
- 30 (1-2), 52-78. DOI: 10.1016/j.cocis.2005.05.007.
- 31 (3) Perry, S. L.; Li, Y.; Priftis, D.; Leon, L.; Tirrell, M. The Effect of Salt on the Complex
- Coacervation of Vinyl Polyelectrolytes. *Polymers* **2014**, *6* (6), 1756-72. DOI:
- 33 10.3390/polym6061756.
- 34 (4) (a) Bettinger, T.; Carlisle, R. C.; Read, M. L.; Ogris, M.; Seymour, L. W. Peptide-mediated
- RNA delivery: a novel approach for enhanced transfection of primary and post-mitotic cells.
- 36 Nucleic Acids Res. **2001**, 29 (18), 3882-91. DOI: 10.1093/nar/29.18.3882. (b) Rhaese, S.; von
- 37 Briesen, H.; Rubsamen-Waigmann, H.; Kreuter, J.; Langer, K. Human serum albumin-
- polyethylenimine nanoparticles for gene delivery. J. Controlled Release 2003, 92 (1-2), 199-208.
- 39 DOI: 10.1016/s0168-3659(03)00302-x. (c) Yasar, H.; Ho, D. K.; De Rossi, C.; Herrmann, J.;
- 40 Gordon, S.; Loretz, B.; Lehr, C. M. Starch-Chitosan Polyplexes: A Versatile Carrier System for
- 41 Anti-Infectives and Gene Delivery. *Polymers* **2018**, *10* (3), 252. DOI: 10.3390/polym10030252.

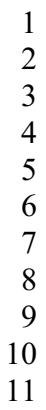
- 1 (5) (a) Stewart, R. J.; Wang, C. S.; Shao, H. Complex coacervates as a foundation for synthetic
- 2 underwater adhesives. Advances in Colloid and Interface Science 2011, 167 (1-2), 85-93. DOI:
- 3 10.1016/j.cis.2010.10.009. (b) Zhao, Q.; Lee, D. W.; Ahn, B. K.; Seo, S.; Kaufman, Y.;
- 4 Israelachvili, J. N.; Waite, J. H. Underwater contact adhesion and microarchitecture in
- 5 polyelectrolyte complexes actuated by solvent exchange. *Nature Materials* **2016**, *15* (4), 407-12.
- 6 DOI: 10.1038/nmat4539.
- 7 (6) Pak, C. W.; Kosno, M.; Holehouse, A. S.; Padrick, S. B.; Mittal, A.; Ali, R.; Yunus, A. A.;
- 8 Liu, D. R.; Pappu, R. V.; Rosen, M. K. Sequence Determinants of Intracellular Phase Separation
- 9 by Complex Coacervation of a Disordered Protein. *Mol. Cell* **2016**, *63* (1), 72-85. DOI:
- 10 10.1016/j.molcel.2016.05.042.
- 11 (7) (a) Pacalin, N.; Leon, L.; Tirrell, M. Directing the phase behavior of polyelectrolyte
- 12 complexes using chiral patterned peptides. The European Physical Journal Special Topics 2016,
- 225, 1805-15. DOI: 10.1140/epjst/e2016-60149-6. (b) Zerze, G. H.; Debenedetti, P.; Stillinger,
- 14 F. Computational Investigation of the Effect of Backbone Chiral Inversions on Polypeptide
- 15 Structure. *Biophys. J.* **2019**, *116* (3), 46A-A. DOI: 10.1016/j.bpj.2018.11.292.
- 16 (8) Tabandeh, S.; Leon, L. Engineering Peptide-Based Polyelectrolyte Complexes with Increased
- 17 Hydrophobicity. *Molecules* **2019**, *24* (5), 868.
- 18 (9) Brangwynne, C. P.; Tompa, P.; Pappu, R. V. Polymer physics of intracellular phase
- 19 transitions. *Nature Physics* **2015**, *11* (11), 899-904. DOI: 10.1038/nphys3532.
- 20 (10) Michaeli, I.; Overbeek, J. T. G.; Voorn, M. J. PHASE SEPARATION OF
- 21 POLYELECTROLYTE SOLUTIONS. Journal of Polymer Science 1957, 23 (103), 443-50.
- 22 DOI: 10.1002/pol.1957.1202310337.
- 23 (11) (a) Kudlay, A.; de la Cruz, M. O. Precipitation of oppositely charged polyelectrolytes in salt
- 24 solutions. J. Chem. Phys. **2004**, 120 (1), 404-12. DOI: 10.1063/1.1629271. (b) Kudlay, A.;
- Ermoshkin, A. V.; de la Cruz, M. O. Complexation of oppositely charged polyelectrolytes:
- 26 Effect of ion pair formation. *Macromolecules* **2004**, *37* (24), 9231-41. DOI: 10.1021/ma048519t.
- 27 (12) (a) Riggleman, R. A.; Fredrickson, G. H. Field-theoretic simulations in the Gibbs ensemble.
- 28 J. Chem. Phys. **2010**, 132 (2), 024104. DOI: 10.1063/1.3292004. (b) Riggleman, R. A.; Kumar,
- 29 R.; Fredrickson, G. H. Investigation of the interfacial tension of complex coacervates using field-
- 30 theoretic simulations. J. Chem. Phys. **2012**, 136 (2), 024903. DOI: 10.1063/1.3674305.
- 31 (13) Perry, S. L.; Sing, C. E. PRISM-Based Theory of Complex Coacervation: Excluded Volume
- versus Chain Correlation. *Macromolecules* **2015**, *48* (14), 5040-53. DOI:
- 33 10.1021/acs.macromol.5b01027.
- 34 (14) Sing, C. E.; Perry, S. L. Recent progress in the science of complex coacervation. *Soft Matter*
- **2020**, *16* (12), 2885-914. DOI: 10.1039/d0sm00001a.
- 36 (15) Radhakrishna, M.; Sing, C. E. Charge Correlations for Precise, Coulombically Driven Self
- 37 Assembly. *Macromolecular Chemistry and Physics* **2016**, *217* (2), 126-36. DOI:
- 38 10.1002/macp.201500278.
- 39 (16) Statt, A.; Casademunt, H.; Brangwynne, C. P.; Panagiotopoulos, A. Z. Model for disordered
- 40 proteins with strongly sequence-dependent liquid phase behavior. J. Chem. Phys. 2020, 152 (7),
- 41 075101. DOI: 10.1063/1.5141095.
- 42 (17) Dignon, G. L.; Zheng, W. W.; Kim, Y. C.; Best, R. B.; Mittal, J. Sequence determinants of
- 43 protein phase behavior from a coarse-grained model. *PLoS Comput. Biol.* **2018**, *14* (1),
- 44 e1005941. DOI: 10.1371/journal.pcbi.1005941.

- 1 (18) Maria Tsanai, P. W. J. M. F., Carsten F. E. Schroer, Paulo C. T. Souza, and; Marrink, S. J.
- 2 Coacervate formation studied by explicit solvent coarse-grain molecular dynamics with the
- 3 Martini model. *Chemical Science* **2021**, *12*, 8521-30.
- 4 (19) Zheng, W. W.; Dignon, G. L.; Jovic, N.; Xu, X. C.; Regy, R. M.; Fawzi, N. L.; Kim, Y. C.;
- 5 Best, R. B.; Mittal, J. Molecular Details of Protein Condensates Probed by Microsecond Long
- 6 Atomistic Simulations. J. Phys. Chem. B **2020**, 124 (51), 11671-9. DOI:
- 7 10.1021/acs.jpcb.0c10489.
- 8 (20) Joseph, J. A.; Reinhardt, A.; Aguirre, A.; Chew, P. Y.; Russell, K. O.; Espinosa, J. R.;
- 9 Garaizar, A.; Collepardo-Guevara, R. Physics-driven coarse-grained model for biomolecular
- phase separation with near-quantitative accuracy. *Nature Computational Science* **2021**, *1* (11),
- 11 732-43. DOI: 10.1038/s43588-021-00155-3.
- 12 (21) Tesei, G.; Schulze, T. K.; Crehuet, R.; Lindorff-Larsen, K. Accurate model of liquid-liquid
- phase behavior of intrinsically disordered proteins from optimization of single-chain properties.
- 14 *Proc. Natl. Acad. Sci. U. S. A.* **2021**, *118* (44), e2111696118. DOI: 10.1073/pnas.2111696118.
- 15 (22) (a) Latham, A. P.; Zhang, B. Maximum Entropy Optimized Force Field for Intrinsically
- 16 Disordered Proteins. J. Chem. Theory Comput. **2020**, 16 (1), 773-81. DOI:
- 17 10.1021/acs.jctc.9b00932. (b) Wu, H.; Wolynes, P. G.; Papoian, G. A. AWSEM-IDP: A Coarse-
- Grained Force Field for Intrinsically Disordered Proteins. J. Phys. Chem. B 2018, 122 (49),
- 19 11115-25. DOI: 10.1021/acs.jpcb.8b05791.
- 20 (23) (a) Nanda, V.; DeGrado, W. F. Simulated evolution of emergent chiral structures in
- 21 polyalanine. Journal of the American Chemical Society 2004, 126 (44), 14459-67. DOI:
- 22 10.1021/ja0461825. (b) Perets, E. A.; Videla, P. E.; Yan, E. C. Y.; Batista, V. S. Chiral Inversion
- 23 of Amino Acids in Antiparallel beta-Sheets at Interfaces Probed by Vibrational Sum Frequency
- 24 Generation Spectroscopy. J. Phys. Chem. B **2019**, 123 (27), 5769-81. DOI:
- 25 10.1021/acs.jpcb.9b04029. (c) Zerze, G. H.; Stillinger, F. H.; Debenedetti, P. G. Effect of
- heterochiral inversions on the structure of a beta-hairpin peptide. *Proteins-Structure Function*
- 27 and Bioinformatics **2019**, 87 (7), 569-78. DOI: 10.1002/prot.25680. (d) Shen, J. X. d-Amino acid
- substituted peptides as potential alternatives of homochiral 1-configurations. *Amino Acids* **2021**,
- 29 53 (2), 265-80. DOI: 10.1007/s00726-021-02947-3.
- 30 (24) Biovia, D.S. (2019) Discovery Studio Visualizer. San Diego.; (accessed 7/31/23).
- 31 (25) Case, D.; Cerutti, D.; Cheatham, T.; Darden, T.; Duke, R.; Giese, T.; Gohlke, H.; Goetz, A.;
- 32 Greene, D.; Homeyer, N. Amber 18 (University of San Francisco). 2017.
- 33 (26) Jo, S.; Kim, T.; Iyer, V. G.; Im, W. CHARMM-GUI: A web-based graphical user interface
- 34 for CHARMM. J. Comput. Chem. 2008, 29 (11), 1859-65. DOI:
- 35 <u>https://doi.org/10.1002/jcc.20945.</u>
- 36 (27) Huang, J.; Rauscher, S.; Nawrocki, G.; Ran, T.; Feig, M.; de Groot, B. L.; Grubmüller, H.;
- 37 MacKerell, A. D. CHARMM36m: an improved force field for folded and intrinsically disordered
- 38 proteins. *Nature Methods* **2016**, *14* (1), 71-3, OriginalPaper. DOI: doi:10.1038/nmeth.4067.
- 39 (28) Berendsen, J.-P. R. a. G. C. a. H. J. C. Numerical integration of the cartesian equations of
- 40 motion of a system with constraints: molecular dynamics of n-alkanes. *Journal of Computational*
- 41 Physics **1977**, 23 (3), 327-41. DOI: https://doi.org/10.1016/0021-9991(77)90098-5.
- 42 (29) (a) Martyna, G. J.; Tobias, D. J.; Klein, M. L. Constant pressure molecular dynamics
- 43 algorithms. The Journal of Chemical Physics 1994, 101 (5), 4177-89. DOI: 10.1063/1.467468
- 44 (accessed 7/31/23). (b) Feller, S. E.; Zhang, Y.; Pastor, R. W.; Brooks, B. R. Constant pressure
- 45 molecular dynamics simulation: The Langevin piston method. *The Journal of Chemical Physics*
- 46 **1995**, 103 (11), 4613-21. DOI: 10.1063/1.470648 (accessed 7/31/2023).

- 1 (30) Darden, T.; York, D.; Pedersen, L. Particle mesh Ewald: An N·log(N) method for Ewald
- 2 sums in large systems. The Journal of Chemical Physics 1993, 98 (12), 10089-92. DOI:
- 3 10.1063/1.464397 (accessed 8/8/2023).
- 4 (31) Martínez, L.; Andrade, R.; Birgin, E. G.; Martínez, J. M. PACKMOL: a package for
- 5 building initial configurations for molecular dynamics simulations. J. Comput. Chem. 2009, 30
- 6 (13), 2157-64. DOI: 10.1002/jcc.21224 From NLM.
- 7 (32) RENARDUS, H. B. a. H. B. a. E. D. a. S. A. a. R. V. a. D. V. a. A. S. a. H. K. a. M.
- 8 GROMACS A PARALLEL COMPUTER FOR MOLECULAR-DYNAMICS SIMULATIONS";
- 9 World Scientific Publishing, 1993.
- 10 (33) Lee, J.; Cheng, X.; Swails, J. M.; Yeom, M. S.; Eastman, P. K.; Lemkul, J. A.; Wei, S.;
- Buckner, J.; Jeong, J. C.; Qi, Y.; et al. CHARMM-GUI Input Generator for NAMD,
- 12 GROMACS, AMBER, OpenMM, and CHARMM/OpenMM Simulations Using the
- 13 CHARMM36 Additive Force Field. *J. Chem. Theory Comput.* **2016**, *12* (1), 405-13. DOI:
- 14 10.1021/acs.jctc.5b00935.
- 15 (34) and, M. A.; and, A. A.; and, C. B.; and, E. B.; and, M. D.; and, S. F.; and, V. G.;
- and, G. G.; and, S. G.; et al. *GROMACS 2023.2 Manual*; Zenodo, 2023. DOI:
- 17 10.5281/zenodo.8134388.
- 18 (35) Hess, B.; Bekker, H.; Berendsen, H. J. C.; Fraaije, J. G. E. M. LINCS: A linear constraint
- solver for molecular simulations. J. Comput. Chem. 1997, 18 (12), 1463-72. DOI:
- 20 https://doi.org/10.1002/(SICI)1096-987X(199709)18:12<1463::AID-JCC4>3.0.CO;2-H.
- 21 (36) Evans, D. J.; Holian, B. L. The Nose–Hoover thermostat. *The Journal of Chemical Physics*
- 22 **1985**, 83 (8), 4069-74. DOI: 10.1063/1.449071 (accessed 8/4/2023).
- 23 (37) Parrinello, M.; Rahman, A. Polymorphic transitions in single crystals: A new molecular
- 24 dynamics method. J. Appl. Phys. 1981, 52 (12), 7182-90. DOI: 10.1063/1.328693 (accessed
- 25 7/27/2023).
- 26 (38) Kabsch, W.; Sander, C. Dictionary of protein secondary structure: pattern recognition of
- 27 hydrogen-bonded and geometrical features. *Biopolymers* **1983**, *22* (12), 2577-637. DOI:
- 28 10.1002/bip.360221211 From NLM.
- 29 (39) (a) Roe, D. R.; Thomas E. Cheatham, I. PTRAJ and CPPTRAJ: Software for
- 30 Processing and Analysis of Molecular Dynamics Trajectory Data. J. Chem.
- 31 *Theory Comput.* **2013**, *9* (7), 3084-95. (b) D.A. Case, K. B., I.Y. Ben-Shalom, S.R. Brozell, D.S.
- 32 Cerutti, T.E. Cheatham, III, V.W.D. Cruzeiro, T.A. Darden, R.E. Duke, G. Giambasu, M.K.
- 33 Gilson, H. Gohlke, A.W. Goetz, R. Harris, S. Izadi, S.A. Iz-mailov, K. Kasavajhala, A.
- 34 Kovalenko, R. Krasny, T. Kurtzman, T.S. Lee, S. LeGrand, P. Li, C. Lin, J. Liu, T. Luchko, R.
- Luo, V. Man, K.M. Merz, Y. Miao, O. Mikhailovskii, G. Monard, H. Nguyen, A. Onufriev, F.
- Pan, S. Pantano, R. Qi, D.R. Roe, A. Roitberg, C. Sagui, S. Schott-Verdugo, J. Shen, C.L.
- 37 Simmerling, N.R. Skrynnikov, J. Smith, J. Swails, R.C. Walker, J. Wang, L. Wilson, R.M. Wolf,
- 38 X. Wu, Y. Xiong, Y. Xue, D.M. York and P.A. Kollman AMBER 2020, University of
- 39 California, San Francisco.
- 40 (40) Schulten, W. H. a. A. D. a. K. VMD: Visual molecular dynamics. J. Mol. Graph. 1996, 14
- 41 (1), 33-8. DOI: https://doi.org/10.1016/0263-7855(96)00018-5.
- 42 (41) Michaud-Agrawal, N.; Denning, E. J.; Woolf, T. B.; Beckstein, O. MDAnalysis: A toolkit
- for the analysis of molecular dynamics simulations. J. Comput. Chem. 2011, 32 (10), 2319-27.
- 44 DOI: https://doi.org/10.1002/jcc.21787.
- 45 (42) Hunter, J. D. Matplotlib: A 2D graphics environment. Computing In Science &
- 46 Engineering **2007**, 9 (3), 90-5.

- 1 (43) Basu, S.; Biswas, P. Salt-bridge dynamics in intrinsically disordered proteins: A trade-off
- between electrostatic interactions and structural flexibility. *Biochimica et Biophysica Acta (BBA)*
- 3 Proteins and Proteomics **2018**, 1866 (5), 624-41. DOI:
- 4 <u>https://doi.org/10.1016/j.bbapap.2018.03.002</u>.
- 5 (44) Voet, D.; Voet, J. G. Biochemistry; John Wiley & Sons Hoboken, NJ, 2011.
- 6 (45) Amadei, A.; Linssen, A. B. M.; Berendsen, H. J. C. Essential dynamics of proteins.
- 7 Proteins: Structure, Function, and Bioinformatics 1993, 17 (4), 412-25. DOI:
- 8 https://doi.org/10.1002/prot.340170408.
- 9 (46) (a) Long, A. W.; Ferguson, A. L. Rational design of patchy colloids via landscape
- engineering. Molecular Systems Design & Engineering 2018, 3 (1), 49-65,
- 11 10.1039/C7ME00077D. DOI: 10.1039/C7ME00077D. (b) Tang, Y.; Bera, S.; Yao, Y.; Zeng, J.;
- Lao, Z.; Dong, X.; Gazit, E.; Wei, G. Prediction and characterization of liquid-liquid phase
- separation of minimalistic peptides. Cell Reports Physical Science 2021, 2 (9), 100579. DOI:
- 14 <u>https://doi.org/10.1016/j.xcrp.2021.100579</u>.
- 15 (47) Hui, T.; Descoteaux, M. L.; Miao, J.; Lin, Y.-S. Training Neural Network Models Using
- 16 Molecular Dynamics Simulation Results to Efficiently Predict Cyclic Hexapeptide Structural
- 17 Ensembles. J. Chem. Theory Comput. **2023**, 19 (14), 4757-69. DOI: 10.1021/acs.jctc.3c00154.
- 18 (48) Hénin, J., Lelièvre, T., Shirts, M. R., Valsson, O., and Delemotte, L. . Enhanced Sampling
- 19 Methods for Molecular Dynamics Simulations. Living Journal of Computational Molecular
- 20 Science 2022, 4 (1), 1583.

- 21 (49) Laio, A.; Parrinello, M. Escaping free-energy minima. Proc. Natl. Acad. Sci. U. S. A. 2002,
- 22 99 (20), 12562-6. DOI: 10.1073/pnas.202427399.
- 23 (50) Tang, P. K.; Khatua, P.; Carnevale, V.; Loverde, S. M. Exploration of the Nucleation
- 24 Pathway for Supramolecular Fibers. *J. Chem. Inf. Model.* **2023**, *63* (8), 2419-26. 25



For Table of Contents Use Only

